frontiers | Frontiers in Earth Science

TYPE Original Research
PUBLISHED 22 August 2022
DOI 10.3389/feart.2022.967572

OPEN ACCESS

EDITED BY
Hao Long,
Nanjing Institute of Geography and Limnology (CAS), China

REVIEWED BY
Xiaomei Nian,
East China Normal University, China
Xianjiao Ou,
Jiaying University, China

*CORRESPONDENCE
T. Tamura,
toru.tamura@aist.go.jp

SPECIALTY SECTION
This article was submitted to Quaternary Science, Geomorphology and Paleoenvironment, a section of the journal Frontiers in Earth Science

RECEIVED 13 June 2022
ACCEPTED 12 July 2022
PUBLISHED 22 August 2022

CITATION
Tamura T, Okazaki H, Naya T, Nakashima R, Nakazato H, Seike K and Okuno J (2022), Luminescence chronology for identifying depositional sequences in an uplifted coast since the Middle Pleistocene, eastern Japan. *Front. Earth Sci.* 10:967572. doi: 10.3389/feart.2022.967572

Luminescence chronology for identifying depositional sequences in an uplifted coast since the Middle Pleistocene, eastern Japan

T. Tamura[1,2,3]*, H. Okazaki[4], T. Naya[1], R. Nakashima[1], H. Nakazato[5], K. Seike[1] and J. Okuno[6]

[1]Geological Survey of Japan, AIST, Tsukuba, Japan, [2]Graduate School of Frontier Science, The University of Tokyo, Kashiwa, Japan, [3]Institute for Space-Earth Environmental Research, Nagoya University, Nagoya, Japan, [4]Fukada Geological Institute, Tokyo, Japan, [5]Institute for Rural Engineering, NARO, Tsukuba, Japan, [6]National Institute of Polar Research, Tachikawa, Japan

Feldspar post-infrared infrared stimulated luminescence (pIRIR) dating is an advantageous trapped-charge dating method concerning late Quaternary sedimentary records for its direct applicability to clastic sediments and wide time coverage. Its application to depositional sequences in various coastal settings potentially improve our understanding of long-term sea-level changes and regional tectonics that the sequences record. The Kanto coastal plain, eastern Japan is situated in a unique tectonic setting near the triple junction of plate boundaries and characterized by extensive development of the Last Interglacial raised marine terrace in contrast to the longer-term subsidence trend. In this article, we document the application of feldspar pIRIR dating to a 35-m-long sediment core collected from the marine terrace in the northeastern Kanto plain and examine how effective its chronology is for identifying depositional sequences related to the relative sea-level fluctuations since the Middle Pleistocene. The sediment core shows a succession of seven facies units, A to G, in ascending order, representing the shallow marine to shelf (units A to C), fluvial to brackish salt marsh (unit D), beach to shoreface (unit E), fluvial to aeolian (unit F), and loess (unit G) sedimentation. According to pre-tests, pIRIR at 225°C after prior infrared stimulated luminescence at 50°C ($pIRIR_{225}$) was chosen as an optimal signal for dating. $pIRIR_{225}$ is characterized by modest anomalous fading with an average g_{2days}-value of 1.8%/decade. Fading-corrected $pIRIR_{225}$ ages are consistent with the stratigraphy. Units A and B are dated as Marine Oxygen Isotope Stage (MIS) 7 and units C to F as MIS 5. However, uncertainties of individual age estimates do not allow further chronological correlation. Instead, using sea-level changes inferred from characteristic facies transitions as additional constraints, units C to F can be correlated to sub-stages in MIS 5. Unit E represents coastal progradation during the MIS 5c sea-level highstand, which refines the date of the marine terrace around the core site as MIS 5c and revises up the rate of the tectonic uplift accordingly. Our results exemplify a successful application of feldspar pIRIR dating for identifying depositional sequences formed in relations to 100-kyr glacial cycles, in which, with

additional information of the sedimentary facies, higher-frequency sequences may be defined.

KEYWORDS

Last Interglacial period, optically stimulated luminescence, post-infrared infrared stimulated luminescence, sea-level changes, tectonics

Introduction

Feldspar post-infrared infrared stimulated luminescence (pIRIR) dating, since it was introduced (Thomsen et al., 2008; Buylaert et al., 2009), has been applied for constraining the chronology of late Quaternary sedimentary records, leading to important findings in geosciences and archeology (e.g., Stevens et al., 2011, 2018; Li and Li, 2012; Buylaert et al., 2013; Arnold et al., 2014; Nian et al., 2016; Li et al., 2017; Westaway et al., 2017; Rizal et al., 2020; Christ et al., 2021). In addition to the direct applicability to the clastic sediment, feldspar pIRIR dating is advantageous for its broad time coverage from several hundred to hundreds of thousands of years (e.g., Thiel et al., 2011; Reimann and Tsukamoto, 2012; Li et al., 2014). Pleistocene sandy depositional sequences in high-energy coastal settings exemplify cases to which feldspar pIRIR dating is ideally applied but are yet to fully benefit from its development even though their accurate chronology potentially refines our knowledge of long-term coastal environments, sea-level changes, and tectonic displacement that they record (e.g., Murray-Wallace and Woodroffe, 2014).

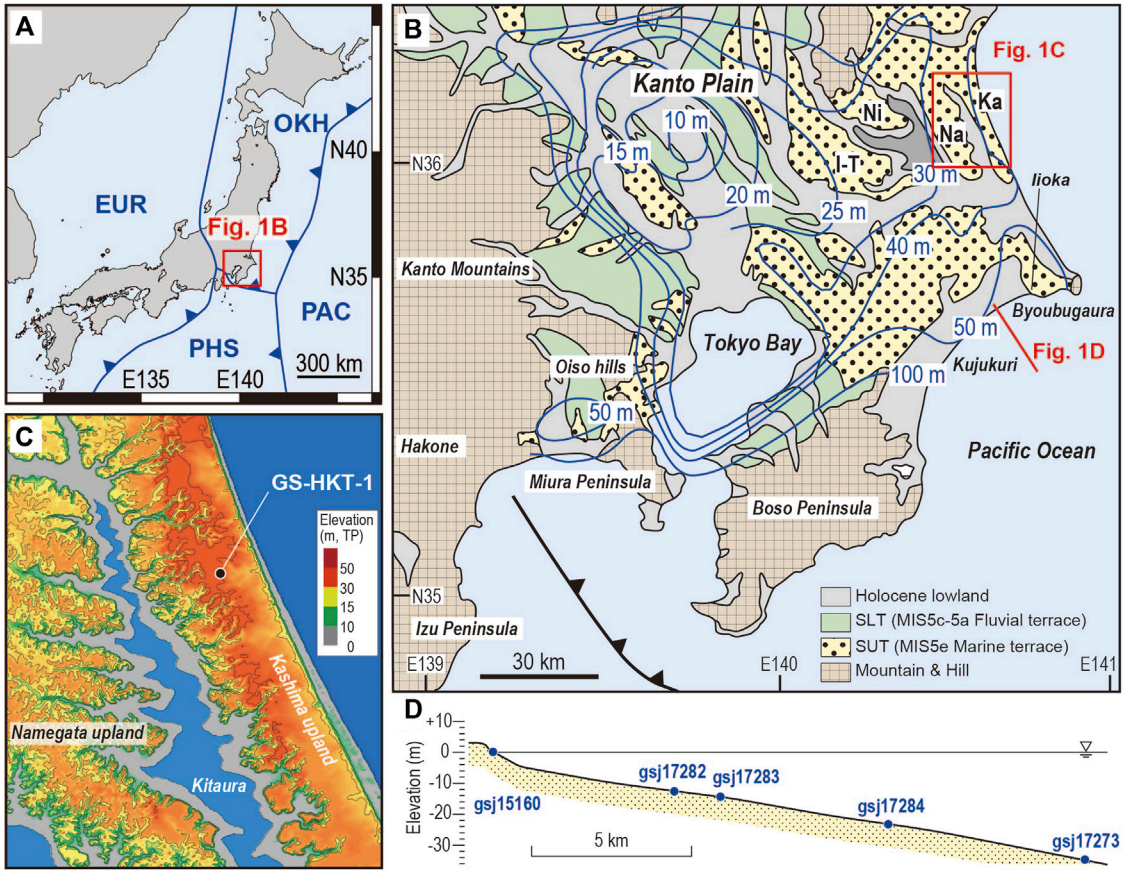

FIGURE 1
(A) Tectonic setting of Japan and the location of the Kanto Plain. **(B)** Landform classification of the Kanto Plain, central Japan. Elevation of the Marine Isotope Stage (MIS) 5e marine terrace (contours shown in blue) is supposed to reflect the tectonic vertical displacement (modified from Kaizuka, 1987). SUT: Shimosa Upper Terrace, SLT: Shimosa Lower Terrace, I–T: Inashiki-Tsukuba upland, Ni: Niihari upland, Na: Namegata upland, Ka: Kashima upland. **(C)** A digital elevation model of the Kashima and Namegata uplands showing the site of core GS-HKT-1 [See location in **(B)**]. The base map is taken from the GSI Map of the Geospatial Information Authority of Japan. **(D)** Cross section across the Kujukuri beach and offshore area [see location in **(B)**]. The positions of five modern sediment samples determined for residual doses are projected onto this single section.

The Kanto plain is a Neogene–Quaternary tectonic basin facing the Pacific coast of central Japan with a 3,000–5,000 m thick accumulation of siliciclastic sediments (e.g., Suzuki, 2002; Takahashi et al., 2005; Suzuki et al., 2011). Since the Middle Pleistocene, the remnant of the basin has been filled with terrigenous and marine deposits under the influence of glacial sea-level cycles to result in depositional sequences referred to as the Shimosa Group (e.g., Tokuhashi and Kondo, 1989; Okazaki et al., 1997). The basin is situated in a unique tectonic setting of the convergent plate margin; it is now covered with the Last Interglacial raised marine terrace that reveals an uplift trend at least over the last 100,000 years in contrast to the longer-term subsidence that resulted in the development of the sedimentary basin (Kaizuka, 1987; Sugai et al., 2013). The depositional sequences in the Kanto plain since the Middle Pleistocene are thus products of the glacial sea-level cycles and tectonic deformation, and with their chronology constrained well, it should improve our understanding of the complicated tectonic history of central Japan and the late Quaternary environmental changes.

Tephrochronology has been constrained well for the Shimosa Group in the southern and western parts of the Kanto plain (Machida and Arai, 2003), close to Quaternary volcanos in the Izu Peninsula and the Hakone and Kanto mountains (Figure 1B). In contrast, tephrochronology in the eastern Kanto plain has been limited owing to fewer tephra layers preserved because of the distance from the source volcanos and high-energy sedimentary environment. Thus, felspar pIRIR potentially refines the chronostratigraphy of the region. Okazaki et al. (2022) determined the pIRIR ages of shallow-marine deposits that comprise the marine terrace at the eastern end of the Kanto plain. The marine terrace was formerly correlated with Marine Oxygen Isotope Stage (MIS) 5e (Sugihara, 1970). These ages, along with a newly identified key tephra, refined the chronology of the terrace as MIS 5c and 5a. Likewise, feldspar pIRIR dating may be further applied to the marine terrace elsewhere and deeper stratigraphy, potentially refining the chronology of the Shimosa Group.

This article presents the application of feldspar pIRIR dating to high-frequency Pleistocene depositional sequences identified in a sediment core from the northeastern Kanto plain. We first test multiple pIRIR signals to select an optimal condition for dating and then discuss the determination of fading rates for correcting the pIRIR ages. The resultant chronology of the sediment core illustrates how effective the corrected pIRIR ages are for defining the depositional sequences formed in relations to glacial sea-level cycles since the Middle Pleistocene.

Study area

The Kanto plain is a coastal plain c. 75 km wide and < +120 m in elevation on the Pacific coast of eastern Japan (Figures 1A,B). It is a relict forearc basin facing the triple junction of plate boundaries that resulted from the subduction of the Pacific and Philippine Sea plates beneath the North American plate to the west and northwest, respectively. Major landforms in the Kanto Plain are Pleistocene uplands and Holocene lowlands. The uplands have two levels: the Shimosa Upper Terrace and the Shimosa Lower Terrace (Sugihara, 1970). The Upper Terrace occurs over the Kanto plain and has been considered the marine terrace formed during the MIS 5e sea-level highstand. The Lower Terrace is generally restricted inland compared to the Upper Terrace and supposed to be the fluvial terrace formed after MIS 5e. The level of the Upper Terrace varies spatially from +10 to +120 m, implying a differing rate of the vertical crustal displacement after MIS 5e (Kaizuka, 1987). Two centers of subsidence to modest uplift are defined in the northwestern part and Tokyo Bay, while a higher-uplift zone occurs along the Pacific coast associated with the northward tilting of the Boso Peninsula (Figure 1B). These variable structures reflect complex tectonics near the triple junction of the plate boundaries (Kaizuka, 1987).

The Quaternary stratigraphy of the Kanto plain is defined by the Lower to Middle Pleistocene Kazusa and Middle to Upper Pleistocene Shimosa groups. The Shimosa Group consists of depositional sequences of fluvial, coastal, and shallow-marine

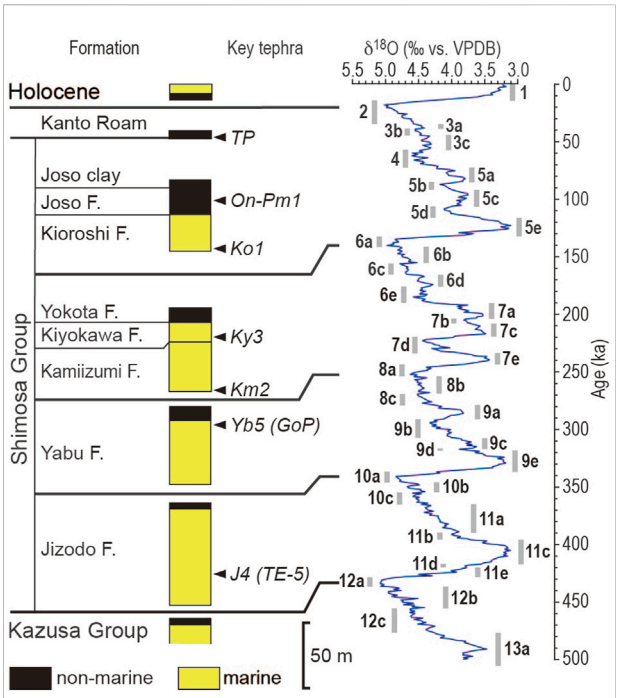

FIGURE 2
Chronostratigraphic chart of the Middle–Upper Pleistocene Shimosa Group and the correlation with the LR04 stack of marine benthic foraminiferal d^{18}O data (Lisiecki and Raymo, 2005) and the marine isotope substages (Railsback et al., 2015) according to Nakazato and Sato. (2001).

sediments. Key tephra layers intercalated in the Shimosa Group provide a well-established tephrochronology in the eastern and southern parts of the Kanto plain, allowing the depositional sequences to be correlated with glacial cycles after MIS 12 (Figure 2; Nakazato and Sato, 2001). The deposits that comprise the marine terrace are referred to as the Kioroshi Formation and have been a subject of detailed sedimentological investigation that allow three-dimensional reconstruction of the sedimentary system (Okazaki and Masuda, 1992; Murakoshi and Masuda, 1992; Ito and O'hara, 1994; Nakazawa et al., 2017). In the eastern Kanto plain, the Kioroshi Formation is characterized by prograded beach–shoreface facies and in places underlying incised-valley facies, being correlated with the sea-level highstand and rise during MIS 5e. In contrast, the central and western parts of the Kioroshi Formation are supposed to represent a large embayment, referred to as Paleo–Tokyo Bay, enclosed by the barrier. This conventional view of the chronology is to be refined at the eastern margin of the Kanto plain, where it is reconstructed as coastal progradation in relations to sea-level oscillations in the later phase of the Last Interglacial period (MIS 5c to 5a) based on a newly identified key tephra, On-Pm1, and a series of pIRIR ages (Okazaki et al., 2022). Moreover, much less has been clarified for sedimentary systems prior to MIS 5e that resulted in the Yokota, Kiyokawa, Kamiizumi, Yabu, and Jizodo formations in descending order (Figure 2). Unconformities that bound these formations are related to the sea-level lowstands in glacial periods, while the relevance of these deposits with the high-frequency sea-level oscillations is yet to be clarified.

The marine terrace in the northeastern Kanto plain is dissected by valleys filled with Holocene sediments and lake waters, being fragmented into several pieces: the Inashiki–Tsukuba, Niihari, Namegata, and Kashima uplands from west to east (Figures 1B,C). The Kioroshi Formation in the Namegata and Kashima uplands represents a prograded barrier system on an open coast, while an embayment is supposed to have been present inland to the barrier (Murakoshi and Masuda, 1992; Nishida and Ito, 2009). The present coast is associated with negligible coastal progradation during the Holocene. Instead, the modern to Holocene analogy of the prograded barrier system is identified in the Kujukuri coast in the southeastern Kanto plain (Figure 1D; Tamura et al., 2008a, 2021).

Methods

Sediment core description and sampling

A sediment core, GS-HKT-1, was obtained on the Kashima upland by using a rotary drilling method with triple tubes. The core site is located 1.8 km inland from the present shoreline and 40.7 m high above the present sea level (Figure 1C). The recovery length and ratio of the core were 35 m and >95%, respectively. The core was halved vertically under controlled red light, and then one side of the halved core was immediately sampled and packed in aluminum bags to prevent further exposure to the light for luminescence dating. Another side of the core was photographed, described, and then used to obtain radiographs with Hitachi X-ray CT-scan Supria Grande. Molluskan shells found in the core were identified and referenced for habitat and ecology according to Okutani (2000). Selected muddy intervals were sampled for diatom analysis. For diatom analysis, smear slides were prepared following the method described in Naya (2019). Smear slides were mounted in an ultraviolet curing resin (NOA 61: Norland Products Inc., refractive index = 1.56). Diatom valves were counted under a light microscope at 1,000x magnification until the total number of valves reached 100.

Sample preparation for luminescence measurements

Luminescence dating was carried out at the Geological Survey of Japan. A total of 16 samples for luminescence dating were prepared under controlled red light to avoid affecting the luminescence signals (Table 1). Sediments within 10 mm from the surface of the halved core were removed and used for measurements of water content and dosimetry. The remaining samples were processed for luminescence measurements. The samples were treated with hydrochloric acid and hydrogen peroxide to remove carbonate and organic matter, respectively. The sand samples were dried and sieved to extract coarse grains 180–250 μm in diameter and then separated using sodium polytungstate liquids of densities 2.58 and 2.53 g/cm^3. The 2.53–2.58 g/cm^3 fraction was taken as K-feldspar coarse grains. A mud sample was processed with a settling cylinder to extract polymineral fine grains of 4–11 μm diameter. Extracted coarse and fine grains were mounted on stainless steel discs to form large (6 mm in diameter) aliquots for luminescence measurements. Modern sand samples collected from the beach and offshore areas of the Kujukuri coast (reported by Tamura et al., 2021; Figure 1D and Table 2) were also measured to estimate the residual doses retained.

Luminescence measurements

Luminescence measurements were performed with a TL-DA-20 Risø TL/OSL reader equipped with infrared (IR) LEDs with the wavelength centered at 850 nm for stimulation and a ^{90}Sr/^{90}Y beta source for laboratory irradiation. Infrared stimulated luminescence (IRSL) from K-feldspar coarse grains and polymineral fine grains through a combination of Schott BG3, BG39, and GG400 filters was measured with a photomultiplier tube.

10.3389/feart.2022.967572

TABLE 1 Details of samples for luminescence dating and estimation of the dose rate.

Sample ID	Lab code	Facies	Depth (m)	Elevation (m)	Water content (%)	U (ppm)	Th (ppm)	K (%)	Rb (ppm)	Cosmic dose rate (Gy/ka)	Total dose rate (Gy/ka)
HKT-1–1	gsj17097	Aeolian/ Fluvial	3.5	37.2	17	0.36	1.77	1.17	41.5	0.13 ± 0.01	2.01 ± 0.14
HKT-1–2	gsj17101	Aeolian/ Fluvial	4.7	36.0	20	0.43	1.9	1.24	46.2	0.11 ± 0.01	2.04 ± 0.14
HKT-1–3	gsj17111	Aeolian/ Fluvial	9.2	31.6	19	0.43	1.94	1.2	44.8	0.07 ± 0.01	1.98 ± 0.14
HKT-1–16	gsj17115	Foreshore	10.6	30.1	21	0.6	2.44	1.24	46.9	0.06 ± 0.01	2.05 ± 0.14
HKT-1–4	gsj17117	Foreshore	11.2	29.5	20	0.59	2.98	1.35	49.5	0.06 ± 0.01	2.18 ± 0.14
HKT-1–5	gsj17123	Upper shoreface	13.5	27.2	26	0.56	2.48	1.61	58.7	0.05 ± 0.01	2.25 ± 0.14
HKT-1–17	gsj17127	Upper shoreface	15.7	25.1	34	0.8	3.06	1.58	80.5	0.04 ± 0.00	2.20 ± 0.14
HKT-1–6	gsj17134	Lower shoreface	19.2	21.5	32	0.83	3.75	1.39	56.1	0.03 ± 0.00	2.12 ± 0.14
HKT-1–7	gsj17139	Marsh to estuary	21.7	19.0	75	6.14	5.69	0.942	53.9	0.03 ± 0.00	2.64 ± 0.13
HKT-1–20	gsj17140	Marsh to estuary	22.2	18.6	44	2.54	3.26	1.16	44.9	0.03 ± 0.00	2.13 ± 0.14
HKT-1–21	gsj17142	Marsh to estuary	23.3	17.5	30	0.68	3.11	1.33	48.3	0.03 ± 0.00	2.04 ± 0.14
HKT-1–8	gsj17143	Shoreface/ Lag	23.6	17.1	31	0.81	4.43	1.32	50.6	0.03 ± 0.00	2.13 ± 0.14
HKT-1–9	gsj17146	Shoreface/ Shelf	25.2	15.6	42	1.06	3.88	1.59	60.5	0.02 ± 0.00	2.19 ± 0.14
HKT-1–10	gsj17150	Shoreface/ Shelf	27.8	13.0	22	0.92	3.41	1.09	39.1	0.02 ± 0.00	2.01 ± 0.14
HKT-1–11	gsj17153	Shoreface/ Shelf	29.1	11.6	25	0.87	3.46	1.11	39.4	0.02 ± 0.00	1.98 ± 0.14
HKT-1–12	gsj17163	Shoreface/ Shelf	34.3	6.4	26	0.74	2.91	1.09	39.9	0.01 ± 0.00	1.89 ± 0.13

TABLE 2 Details of the modern samples collected in the Kujukuri beach and offshore areas. Equivalent doses (D_e) determined are considered as residual doses.

Site	Lab code	Latitude	Longitude	Water depth (m)	D_e from $pIRIR_{225}$ (Gy)	De from $pIRIR_{290}$ (Gy)
Katakai	gsj15160	N35°32′28.2″	E140°27′55.8"	0	4.05 ± 0.36	11.93 ± 1.66
BS9	gsj17282	N35°37′42.1″	E140°37′13.9"	13	10.25 ± 0.62	27.28 ± 1.08
BS10	gsj17283	N35°37′42.3″	E140°40′16.6″	14	10.98 ± 0.25	29.09 ± 1.44
BS23	gsj17284	N35°35′11.9″	E140°41′48.5"	23	11.34 ± 0.34	29.27 ± 1.47
BS34	gsj17273	N35°32′40.0″	E140°45′39.4″	34	7.53 ± 0.62	23.92 ± 1.60

The modified single aliquot-regenerative (SAR) protocol of pIRIR measured at various temperatures after a prior IRSL at 50°C was applied to K-feldspar coarse grains and polymineral fine grains (Table 3; Thomsen et al., 2008; Buylaert et al., 2009; Reimann and Tsukamoto, 2012). To select an optimal signal for dating, we examined four pIRIR signals, measured at 200, 225, 260, and 290°C, referred to here as $pIRIR_{200}$, $pIRIR_{225}$, $pIRIR_{260}$, and $pIRIR_{290}$, respectively. The pIRIR signals were sampled every 0.1 s for 200 s, and the net signal was derived from the integral of the first 2.0 s of the signal after subtracting the background estimated from the last 20 s of the signal. Preheat was given for 60 s with temperatures at 30°C higher than the measurement temperatures of pIRIR.

TABLE 3 Summary of the pIRIR single-aliquot regenerative dose protocol used in this study.

Step	$pIRIR_{200}$ and $pIRIR_{225}$	Signal		$pIRIR_{260}$ and $pIRIR_{290}$	Signal
1	Preheat at 200 or 255°C for 60 s	—	—	Preheat at 290 or 320°C for 60 s	—
2	IR stimulation at 50°C for 200 s	—	—	IR stimulation at 50°C for 200 s	—
3	IR stimulation at 200 or 225°C for 200 s	Lx	—	IR stimulation at 260 or 290°C for 200 s	Lx
4	Test dose	—	—	Test dose	—
5	Preheat at 200 or 255°C for 60 s	—	—	Preheat at 290 or 320°C for 60 s	—
6	IR stimulation at 50°C for 200 s	—	—	IR stimulation at 50°C for 200 s	—
7	IR stimulation at 200 or 225°C for 200 s	Tx	—	IR stimulation at 260 or 290°C for 200 s	Tx
8	Dose and return to step 1	—	—	IR stimulation at 295 or 325°C for 200 s*	—
9	—	—	—	Dose and return to step 1	—

To select an optimal protocol for dating, bleaching experiments and dose recovery tests were practiced with different signals for the selected samples. Six aliquots for each protocol were exposed to artificial sunlight for 4 h in a UVACUBE 400 chamber (Hönle) with a SOL 500 lamp module. After bleaching, three aliquots were dosed by an expected equivalent dose of 200–300 Gy and then used for a dose recovery test; the remaining aliquots were used to estimate the residual dose. Dose recovery was assessed after subtracting the residual dose from the recovered dose. The preliminary ages of sample gsj17123 using different signals were also determined following the procedure described below, except that three replicates of aliquot were integrated for each condition.

With the optimal pIRIR signal, the mean value of the equivalent dose was determined from the measurements of six replicates of medium aliquots (6 mm in diameter) without subtracting the residual dose. In the SAR protocol, four or five regeneration points and a replicate of the second point were measured and data with recycling ratios outside 1.0 ± 0.1 were rejected. Fading tests were also performed on aliquots after equivalent dose measurement to determine the fading rates after Auclair et al. (2003). The results of the fading tests were integrated for all aliquots of both the individual sample and all samples, obtaining the individual and average fading rates, expressed as the g_{2days}-value or dimensionless density of recombination centers, ρ'.

Dose-rate and age determination

The environmental dose rate was determined using the DRAC program of Durcan et al. (2015) based on contributions of both natural radionuclides in sediments and cosmic rays. The concentrations of K were measured by inductively coupled plasma optical emission spectrometry and those of U, Th, and Rb by inductively coupled plasma mass spectrometry; these results were converted to dose rates by applying the conversion factors of Adamiec and Aitken (1998). The attenuation factors used for beta and alpha rays were based on Mejdahl (1979) and Bell (1980), respectively. We used a-values of 0.110 ± 0.005 and 0.15 ± 0.05 for polymineral fine grains and K-feldspar coarse grains, respectively (Balescu and Lamothe, 1994; Kreutzer et al., 2014). The water content was also considered for the dose rate determination based on the measured value with uncertainties of 5%. Cosmic dose rates were calculated according to Prescott and Hutton (1994). D_e values were then divided by the environmental dose rate to obtain uncorrected ages. For uncorrected ages, fading correction was carried out with the individual and average ρ' according to Huntley and Lian (2006) and Kars et al. (2008) and using the R Luminescence package (Kreutzer et al., 2012; Fuchs et al., 2015). All ages are expressed relative to AD 2020.

Results

Sedimentary facies

Seven sedimentary facies units A to G, in ascending order, are defined in core GS-HKT-1 (Figure 3, Supplementary Figures S1, S2). Unit A occurs at depths of 28.5–35.0 m and is very fine to fine sand with a horizontal to low-angle cross lamination. The low-angle cross lamination in places defines minor truncation surfaces. The unit contains pebble-sized mud clasts at its basal part and generally lacks mollusk shells and bioturbation except for escape structures at depths of 28.20–28.90 m. A pebble-to-granule layer 3 cm thick occurs on an erosion surface at 30.65 m, dividing the unit into two subunits A-1 and A-2; these subunits have similar features.

Unit B gradually overlies unit A and is identified at depths of 25.85–28.50 m. This unit is very fine to fine sand containing abundant mollusk shells and granules. Horizontal to low-angle cross lamination with truncation surfaces is recognized in radiographs. The upper part in contrast is heavily bioturbated

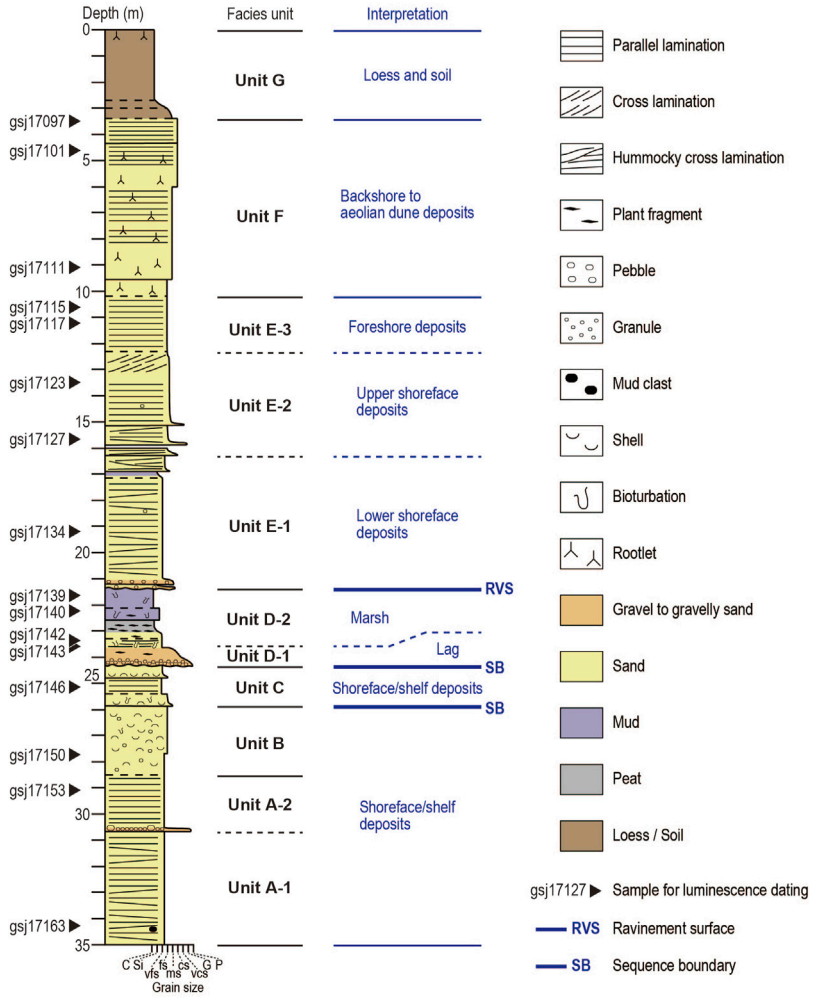

FIGURE 3
Columnar sections of core GS-HKT-1 with definition and interpretation of units A to G, in ascending order and bounding surfaces. Sixteen sediment samples were collected for luminescence dating.

and contains condensed shell beds. Mollusk shells identified in unit B include *Mactra chinensis*, *Mercenaria stimpsoni*, *Nitidotellina minuta*, *Solen strictus*, *Cyclocardia ferruginea*, *Limopsis tokaiensis*, *Acila insignis*, *Siphonalia fusoides*, *Jupiteria* (Saccella) *confusa*, and *Fulvia mutica*. These species live on the sandy seafloor of shallow marines to shelf (Supplementary Table S1; Okutani, 2000). The trace fossil *Bichordites* is identified at depths of 28.00–28.20 m.

Unit C is medium to very fine sand with mollusk shells, defining the core interval from 24.32 to 25.85 m deep. The unit erosionally overlies unit B and consists of two normally graded layers. These layers are characterized by a basal erosion surface and shell-rich layer, normal grading from very fine to medium sand to fine to very fine sand, and well-defined horizontal to low-angle cross lamination with truncation surfaces in the upper part. Mollusk shells identified are species that inhabit the sandy seafloor of shallow marines to shelf, including *Antalis weinkauffi*, *Cyclocardia ferruginea*, *Glycymeris yessoensis*, and *Spisula sachalinensis*. Trace fossils *Bichordites* and *Ophiomorpha* occur at depths of 25.6–25.7 and 25.3 m, respectively.

Unit D occurs at the interval 21.35–24.32 m deep. The unit comprises variable layers that commonly contain plant fragments, and further divided into subunits D-1 and D-2. The subunit D-1, constituting the lower part of unit D, is a gravelly sand 60 cm thick that erosionally overlies unit C. This layer is normally graded from massive coarse sand with granules and pebbles to medium sand with high-angle cross lamination. The graded layer is then conformably overlain by a succession of disturbed centimeter-scale alternations of very fine sand and mud 35 cm thick, massive very fine sand 30 cm thick, and dark-gray peaty mud 40 cm thick, in ascending order. These layers contain plant roots and rootlets. The rest of unit D is subunit D-2.

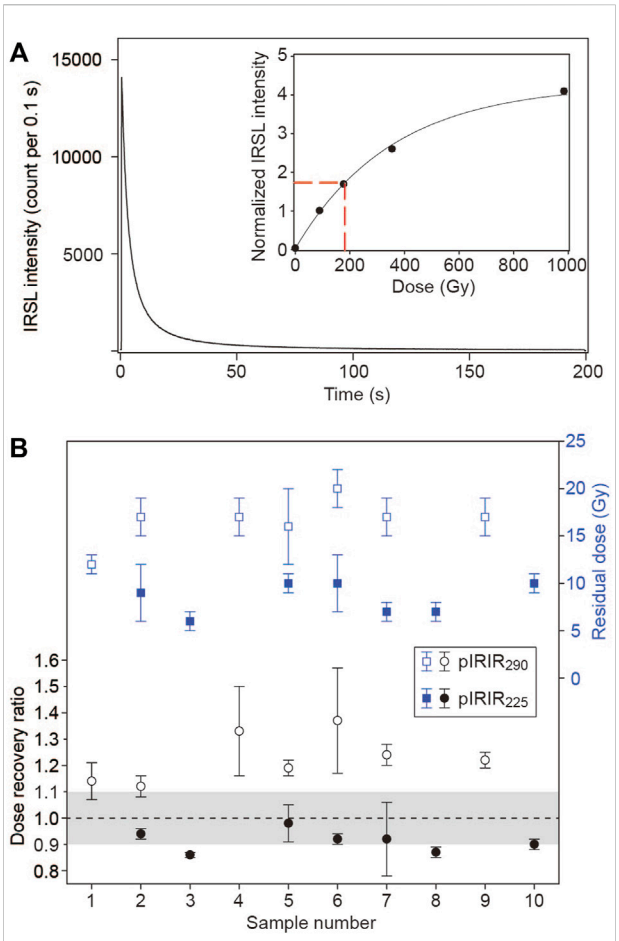

FIGURE 4
(A) Natural decay curve and a dose-response curve (inset) of $pIRIR_{225}$ of K-feldspar coarse grains in sample gsj17123. **(B)** Results of the dose-recovery test and observed residual dose for $pIRIR_{225}$ and $pIRIR_{290}$ in selected samples. 1: gsj17097, 2: gsj17101, 3: gsj17111, 4: gsj17115, 5: gsj17123, 6: gsj17134, 7: gsj17139, 8: gsj17142, 9: gsj17143, 10: gsj17153.

Subunit D-2 is a gray muddy layer 125 cm thick that is graded from sandy silt to clay, erosionally overlying the dark-gray peaty mud of subunit D-1. The lower part of the gray muddy layer is heavily bioturbated, and some burrows are identified as *Ophiomorpha*. In contrast, the upper part is characterized by less dense but larger sandy burrows of *Spongeliomorpha* that appear to have infiltrated from the overlying layer, representing *Glossifungites* Ichnofacies. Diatom valves are found in the peaty mud and gray muddy layer. The peaty mud contains freshwater species, such as *Aulacoseira* spp., *Eunotia* spp., and *Staurosira* spp. The gray muddy layer in contrast is dominated by brackish to marine species such as *Paralia sulcata* and *Pseudopodosira kosugii*, with a larger fraction of freshwater species such as *Staurosira* spp. in the upper part.

Unit E is identified at depths of 21.35–10.20 m. The unit erosionally overlies unit D and defines an upward-coarsening sandy interval. It is divided into subunits E-1, E-2, and E-3, in ascending order. Subunit E-1 constitutes the interval from depths of 16.29–21.35 m. The basal part of the subunit E-1 comprises two poorly sorted layers of very fine sand to granules with angular basal erosion surfaces. These two layers are 5 and 10 cm thick, respectively, bounded by a massive mud layer 5 cm thick. The basal layers are gradually overlain by the rest of subunit E-1 that coarsens upward from very fine sand to very fine-to-fine sand and shows a well-defined horizontal to low-angle cross lamination with a few burrows. The trace fossil *Ophiomorpha* is identified at a depth of 20.50 m. Similar to units A and B, the low-angle cross lamination defines minor truncation surfaces in places. Subunit E-2 is fine to medium sand identified at depths of 12.30–16.29 m, abruptly overlying subunit E-1. The subunit comprises layers characterized by low- to high-angle cross lamination, basal erosion surface, and lags of granules to very coarse sand. Generally, bioturbation is not evident and lamination is well-defined. Subunit E-3 is fine to medium sand with well-defined horizontal lamination, occurring at depths of 10.20–12.30 m.

Unit F is fine to very coarse sand identified at depths of 3.40–10.20 m and gradually overlies unit E-3. This unit generally exhibits rootlets while it varies from massive, through bioturbated, to horizontally laminated with concentrations of heavy minerals. Unit G spans from the ground surface to a depth of 3.40 m. The unit is brownish, massive sandy silt to clay with the lower part 70 cm thick, which defines a transitional interval with an upward decrease in sand content. Rootlets are observed just below the ground surface.

Seven facies units identified in core GS-HKT-1 reveal changes of sedimentary environments; the core site experienced sedimentation in shelf to coastal environments, interrupted with an episode of fluvial to marsh environments, and then was capped with aeolian sedimentation. All of the mollusk shells identified in units B and C are indicative of sandy seafloor environments from the shoreface to shelf. These units, as well as unit A and subunit E-1, show low-angle cross stratification that represents hummocky or swaly cross-stratification of storm deposits (Harms et al., 1975; Leckie and Walker, 1982). According to these features, units A to C and subunit E-1 are interpreted to have been formed by storm processes in the sandy shoreface to shelf. Similar deposits have also been reported from the modern and Holocene shoreface and the shelf off the Kujukuri coast (Figure 1B; Tamura et al., 2007; Nishida et al., 2020). Unit E shows a vertical sandy succession of hummocky or swaly cross-stratification (subunit E-1), high-angle cross lamination (subunit E-2), and a well-defined horizontal lamination (subunit E-3), in ascending order, along with a coarsening upward trend. The high-angle cross stratification and horizontal lamination are interpreted as results of the dune migration in the upper shoreface and beachface sedimentation in the foreshore, respectively. Thus, unit E represents a shoaling

10.3389/feart.2022.967572

TABLE 4 Results of the dose-recovery test and preliminary dating of sample gsj17123 with different pIRIR signals. DRR = dose-recovery ratio, D_e = equivalent dose, ρ′ = dimensionless density of recombination centers.

Signal	DRR	Total dose rate (Gy/ka)	De (Gy)	Uncorrected age (ka)	g2days-value (%/decade)	ρ′	Corrected age (ka)
$pIRIR_{200}$	0.93 ± 0.05	2.25 ± 0.14	179 ± 7	80 ± 6	1.1 ± 0.8	6.9E-07 ± 5.4E-07	93 ± 7
$pIRIR_{225}$	0.98 ± 0.07	2.25 ± 0.14	202 ± 3	90 ± 6	1.0 ± 0.4	6.8E-07 ± 2.7E-07	106 ± 8
$pIRIR_{260}$	1.02 ± 0.07	2.25 ± 0.14	202 ± 5	90 ± 6	0.4 ± 0.2	2.9E-07 ± 1.4E-07	96 ± 8
$pIRIR_{290}$	1.19 ± 0.03	2.25 ± 0.14	229 ± 38	102 ± 18	0.9 ± 0.8	6.4E-07 ± 5.7E-07	117 ± 9

upward succession from the lower shoreface to beach environments (e.g., Clifton, 2006; Isla et al., 2020). Unit D, in contrast to units A to C and E, shows evidence for deposition in freshwater and brackish water environments, most notably from diatoms. Subunit D-1 is interpreted as fluvial lag deposits as it contains plant fragments and rootlets and the coarsest gravels in core GS-HKT-1 with no marine evidence, clearly eroding into the underlying marine deposits of unit C. Freshwater diatoms identified in the basal part of subunit D-2 indicates a marsh environment, and the upward increase of brackish water diatom toward the gray muddy layer is inferred to reflect an increasing influence of saltwater in the marsh environment. Unit F is interpreted to have been deposited in terrigenous environments with aeolian processes as it contains rootlets with no evidence for marine sedimentation. Unit G corresponds to the Younger Kanto Loam, a mixture of loess and volcanic dust and its uppermost part grades to the soil.

Luminescence properties, dose rate, and uncorrected age

Bright pIRIR signals are observed from K-feldspar coarse grains and polymineral fine grains, and the dose-response curves are well-defined (Figure 4A). Dose recovery tests of four pIRIR signals with different temperatures of measurement and preheat for sample gsj17123 yielded variable results (Table 4). The $pIRIR_{290}$ is characterized by a dose recovery ratio markedly higher than 1.1, while the other three signals yielded acceptable ratios within 1.0 ± 0.1 with that of $pIRIR_{200}$ slightly lower. This observation is also confirmed for other selected samples by testing their dose recover ratios of $pIRIR_{225}$ and $pIRIR_{290}$ (Figure 4B). Preliminary dating of sample gsj17123 results in similar uncorrected and corrected ages from $pIRIR_{225}$ and $pIRIR_{260}$. Ages from $pIRIR_{200}$ and $pIRIR_{290}$ are younger and older than those of $pIRIR_{225}$ and $pIRIR_{290}$, respectively, possibly reflecting the trend of the dose recovery ratio. Measurements of the modern sand in the Kujukuri coast indicate that a higher residual dose is retained for $pIRIR_{290}$ than $pIRIR_{225}$ (Table 2), suggesting that the older age of $pIRIR_{290}$ partly owes to the residual dose. The higher residual dose of $pIRIR_{290}$ is also identified in measurements of the selected samples after the 4-h bleaching experiment. These results indicate that $pIRIR_{225}$ and $pIRIR_{260}$ are more suitable for dating than $pIRIR_{200}$ and $pIRIR_{290}$. For its broader application, $pIRIR_{225}$ is used here for further dating.

Natural $pIRIR_{225}$ signals of all the samples are well below the saturation level, and the modified SAR protocol reasonably yields the D_e values. The mean D_e value determined for an individual sample generally decreases upward in the core consistently with the stratigraphy (Table 5). The dose rate

TABLE 5 pIRIR$_{225}$ age estimates. n = the number of aliquots used for age estimation, D_e = equivalent dose, ρ′ = dimensionless density of the recombination centers.

Sample ID	Lab code	Facies	Depth (m)	Elevation (m)	Total dose rate (Gy/ka)	n	De (Gy)	Uncorrected age (ka)	g_{2days}-value (%/decade)	ρ′	Corrected age (ka)
HKT-1–1	gsj17097	Aeolian/Fluvial	3.5	37.2	2.01 ± 0.14	5	149 ± 3	74 ± 5	3.5 ± 0.5	2.37E-06 ± 3.79E-07	104 ± 9
HKT-1–2	gsj17101	Aeolian/Fluvial	4.7	36.0	2.04 ± 0.14	6	170 ± 4	83 ± 6	1.8 ± 0.5	1.21E-06 ± 3.32E-07	117 ± 11
HKT-1–3	gsj17111	Aeolian/Fluvial	9.2	31.6	1.98 ± 0.14	6	180 ± 3	91 ± 6	1.9 ± 0.5	1.30E-06 ± 3.39E-07	127 ± 11
HKT-1–16	gsj17115	Foreshore	10.6	30.1	2.05 ± 0.14	6	169 ± 3	83 ± 6	-0.2 ± 0.5	-1.18E-07 ± 3.34E-07	117 ± 10
HKT-1–4	gsj17117	Foreshore	11.2	29.5	2.18 ± 0.14	6	172 ± 7	79 ± 6	1.9 ± 0.5	1.28E-06 ± 3.34E-07	110 ± 13
HKT-1–5	gsj17123	Upper shoreface	13.5	27.2	2.25 ± 0.14	6	178 ± 6	79 ± 6	1.9 ± 0.5	1.30E-06 ± 3.45E-07	111 ± 14
HKT-1–17	gsj17127	Upper shoreface	15.7	25.1	2.20 ± 0.14	5	189 ± 6	86 ± 6	1.9 ± 0.5	1.30E-06 ± 3.32E-07	117 ± 11
HKT-1–6	gsj17134	Lower shoreface	19.2	21.5	2.12 ± 0.14	6	165 ± 3	78 ± 5	1.5 ± 0.5	1.04E-06 ± 3.36E-07	106 ± 8
HKT-1–7	gsj17139	Marsh to estuary	21.7	19.0	2.64 ± 0.13	6	192 ± 3	73 ± 4	2.2 ± 0.5	1.52E-06 ± 3.62E-07	101 ± 6
HKT-1–20	gsj17140	Marsh to estuary	22.2	18.6	2.13 ± 0.14	6	194 ± 3	91 ± 6	1.7 ± 0.5	1.14E-06 ± 3.55E-07	129 ± 10
HKT-1–21	gsj17142	Marsh to estuary	23.3	17.5	2.04 ± 0.14	6	190 ± 3	93 ± 6	1.9 ± 0.5	1.27E-06 ± 3.40E-07	130 ± 10
HKT-1–8	gsj17143	Lag	23.6	17.1	2.13 ± 0.14	6	182 ± 3	86 ± 6	1.6 ± 0.5	1.05E-06 ± 3.32E-07	120 ± 9
HKT-1–9	gsj17146	Shoreface/Shelf	25.2	15.6	2.19 ± 0.14	6	211 ± 3	96 ± 6	2.0 ± 0.5	1.38E-06 ± 3.35E-07	136 ± 10
HKT-1–10	gsj17150	Shoreface/Shelf	27.8	13.0	2.01 ± 0.14	6	328 ± 5	163 ± 11	1.8 ± 0.5	1.23E-06 ± 3.68E-07	242 ± 19
HKT-1–11	gsj17153	Shoreface/Shelf	29.1	11.6	1.98 ± 0.14	6	310 ± 13	156 ± 13	2.1 ± 0.5	1.44E-06 ± 3.35E-07	230 ± 32
HKT-1–12	gsj17163	Shoreface/Shelf	34.3	6.4	1.89 ± 0.13	6	288 ± 7	152 ± 11	2.3 ± 0.4	1.51E-06 ± 3.35E-07	220 ± 21
—	—	—	—	—	—	—	—	(Average)	1.8 ± 0.1	1.3E-06 ± 8.6E-08	—

10.3389/feart.2022.967572

10.3389/feart.2022.967572

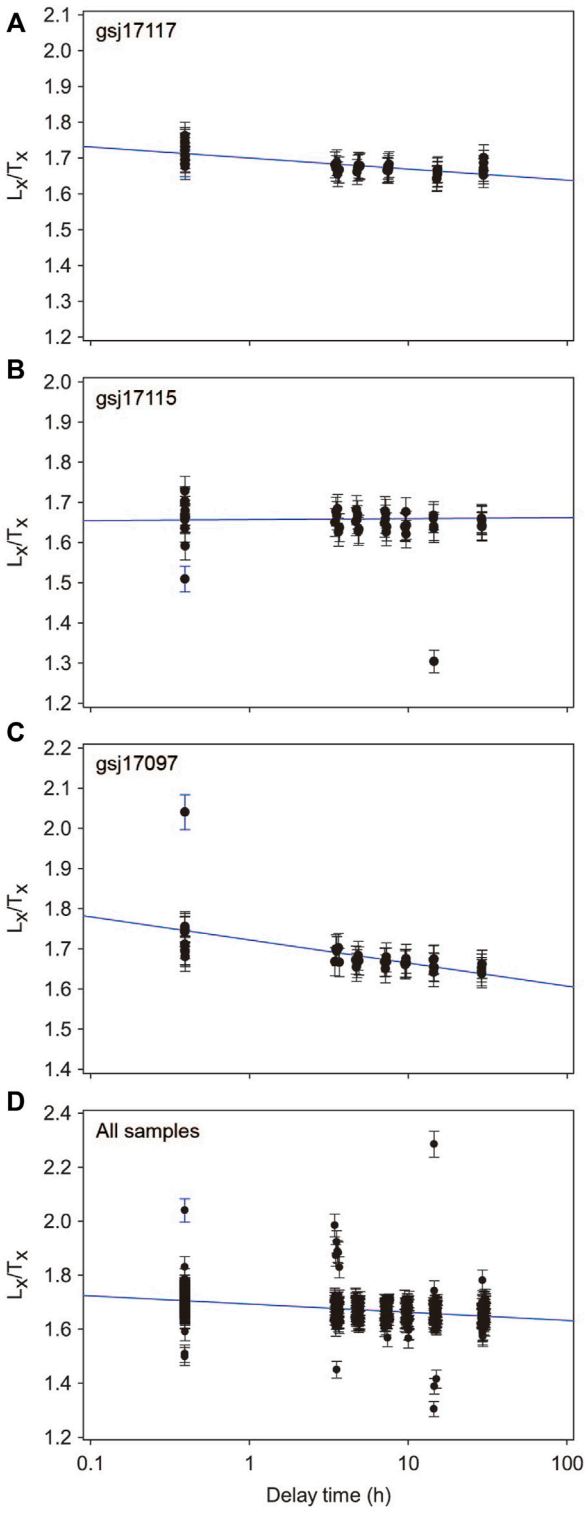

FIGURE 5
Fading test results of pIRIR$_{225}$ integrating all aliquots of **(A)** samples gsj17117, **(B)** gsj17115, and **(C)** 17,097, and **(D)** all of the 16 samples measured here. The result on gsj17117 exemplifies a fading rate close to the average of all samples, while the fading rates of samples gsj17115 and 17,097 are the lowest and highest values of the 16 samples, respectively.

is consistent in coarse-grain samples, ranging from 1.89 to 2.25 Gy/ka, with a slightly higher value of 2.64 Gy/ka for fine grain sample gsj17139. As a result, uncorrected ages are consistent with the stratigraphy. In units E and F, uncorrected ages range between 74 and 91 ka with a few slight reversals, defining no discernible trend. Four uncorrected ages in unit D are slightly older than those in units E and F on average, and an uncorrected age in unit C is slightly further older. A large gap is identified between units B and C; three uncorrected ages in units A and B are 152–163 ka, considerably older than those in the overlying units.

Fading rate and corrected age

Modest anomalous fading is observed in the fading test (Figure 5). In 14 samples, except for samples gsj17097 and 17115, a decrease of luminescence intensity with the time since irradiation, or delay time, is identified and fitted well to define the g_{2days}-value and ρ' (Figure 5A). The g_{2days}-values calculated for these samples are characterized by a narrow range, 1.5–2.2, and centered on 1.8 ± 0.1, a value determined by fitting the results from the aliquots of 16 samples (Figure 5D, Figure 6A); ρ′ shows similar variations to the g_{2days}-value (Figure 6B). Furthermore, there is no vertical trend of the fading rate represented by the g_{2days}-value and ρ' (Table 5). Measurements of samples gsj17097 and 17115 yielded outlier fading rates, reflecting the regression distorted by a few exceptional L_x/T_x values (Figures 5B,C). The fitting of all aliquots, although containing such exceptional values (Figure 5D), is averaged to result in a similar fading rate to that of samples with no exceptional plots (Figure 5A). Although the origin of the exceptional L_x/T_x values is unclear, the fitting of all the aliquots is considered to minimize their effect.

Two series of corrected ages are obtained assuming the fading rate determined for an individual sample or the average fading rate for all samples (Table 5; Figures 6C,7). In general, both series show negligible offsets from each other except for samples gsj17097 and 17115, characterized by outlier fading rates. The corrected age of gsj17097 with the individual rate is remarkably older than the other, leading to a remarkable age reversal. No fading correction is possible for gsj17115 with its negative fading rate, and the uncorrected age defines an age reversal with the three corrected ages in the upper part of the core. The corrected ages with the average fading rate in contrast define a sequence consistent with the stratigraphy when taking into account the errors and thus are considered the final age estimate here.

The final corrected ages indicate an approximate depositional timing of the sediment succession. Five corrected ages from unit E range from 106 to 117 ka with the youngest estimate identified for sample gsj17134, the lowest in the unit. Three corrected ages in unit F are 104–127 ka and younger upward. Sample gsj17111 is dated older than the ages in unit E below and thus appears to be

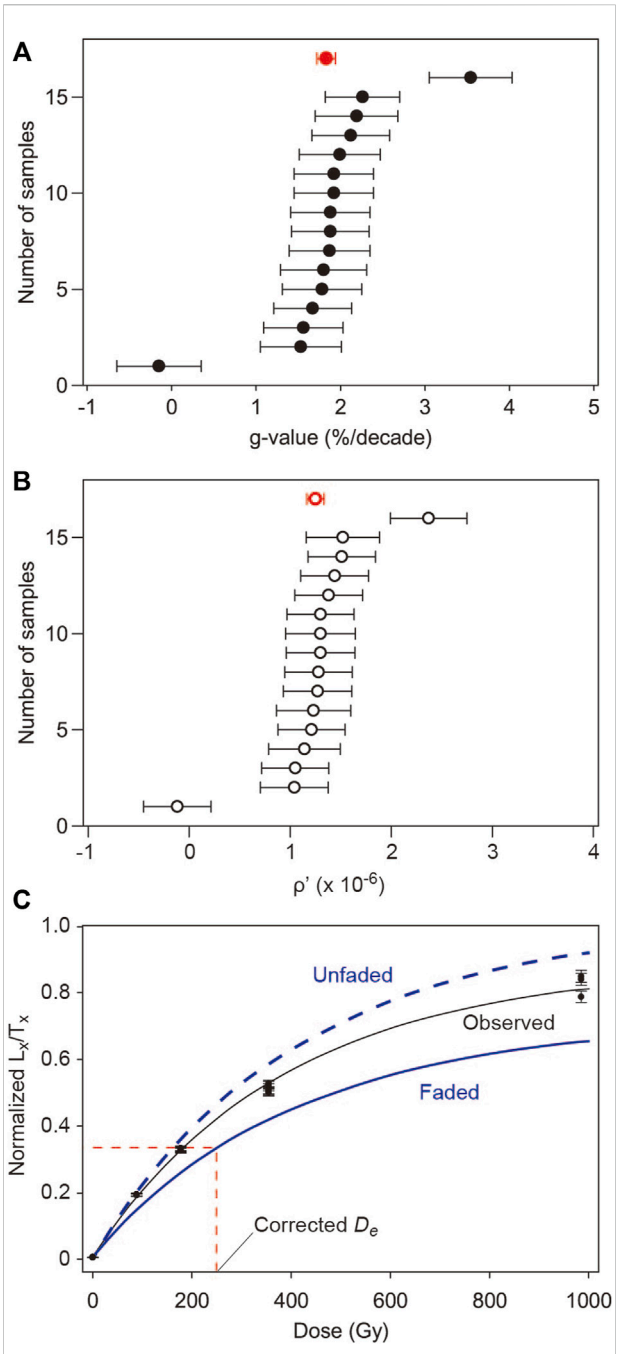

FIGURE 6
(A) Cumulative distribution of the g_{2days}-value determined for an individual sample. A red point shows the average value for all the samples. **(B)** Cumulative distribution of the ρ', dimensionless density of recombination centers. A red point shows the average value for all samples. **(C)** An example of fading correction with measured, unfaded, and faded dose-response curves for the $pIRIR_{225}$ signal from sample gsj17123.

slightly overestimated. The corrected ages in units E and F indicate that these units were deposited sometime from MIS 5e to 5c. The four corrected ages in unit D are consistent with the stratigraphy; the only fine grain sample gsj17139 is dated to MIS 5c to 5d, while the remaining three coarse-grain samples are dated to MIS 5d to 6a. A corrected age in unit C is dated to the begining of MIS5e to 6a. A large hiatus is defined by the corrected ages between units B and C, approximately corresponding to the duration of MIS 6. Three ages in units A and B are associated with larger errors and roughly correlated with MIS 8a to 7a.

Discussion

Identification of depositional sequences

The corrected $pIRIR_{225}$ ages are associated with uncertainties that do not allow a detailed correlation with the marine isotope sub-stages. However, the series of ages are integrated with information of sea-level changes revealed by the facies succession as additional constraints for supporting further chronological interpretation. Three key features of sedimentary facies in core GS-HKT-1 indicative of the sea-level changes include the facies shift from units C to D, internal facies changes in unit D, and the facies shift from units D to E. The transition from units C to D reveals a change from a shallow marine to fluvial environments, which is caused by a relative sea-level fall. The erosional base of unit D is considered an unconformity formed by fluvial erosion. The vertical succession of unit D then represents a shift from a fluvial environment to brackish salt marsh, inferred from units D-1 and D-2, respectively. This shift is caused by transgression owing to a relative sea-level rise. Unit D is likely a fill of an incised-valley dissected onto the unconformity. The deposition of unit D-2 is followed by further transgression and wave erosion in an open marine environment that resulted in the ravinement surface (Nummedal and Swift, 1987), corresponding to the basal erosion surface of unit E. Such facies succession is ubiquitously identified in post-glacial deposits along the Pacific coast of eastern Japan (e.g., Tamura et al., 2003; Tamura and Masuda, 2005). Unit E is a shoaling-upward succession representing coastal progradation during the sea-level highstand with possible minor sea-level fluctuations. These key features of sedimentary facies above unit B indicate sea-level fluctuations characterized by a succession of a fall, rise, and highstand.

The inferred sea-level oscillation allows the correlations of units C to F with the sub-stages in MIS 5 (Figure 8; Waelbroeck et al., 2002). The basal erosion surface of unit C represents a large hiatus spanning MIS 6 and is considered the ravinement surface finally formed by wave erosion in relation to the sea-level rise and transgression from MIS 6a to 5e. Unit C, with a $pIRIR_{225}$ age with errors ranging from 6a to 5e, is thus considered to have been deposited in MIS 5e. The deposition of unit D then occurred between MIS 5e and 5c. Its basal unconformity was thus formed by the sea-level fall from MIS 5e to 5d. The subsequent sea-level

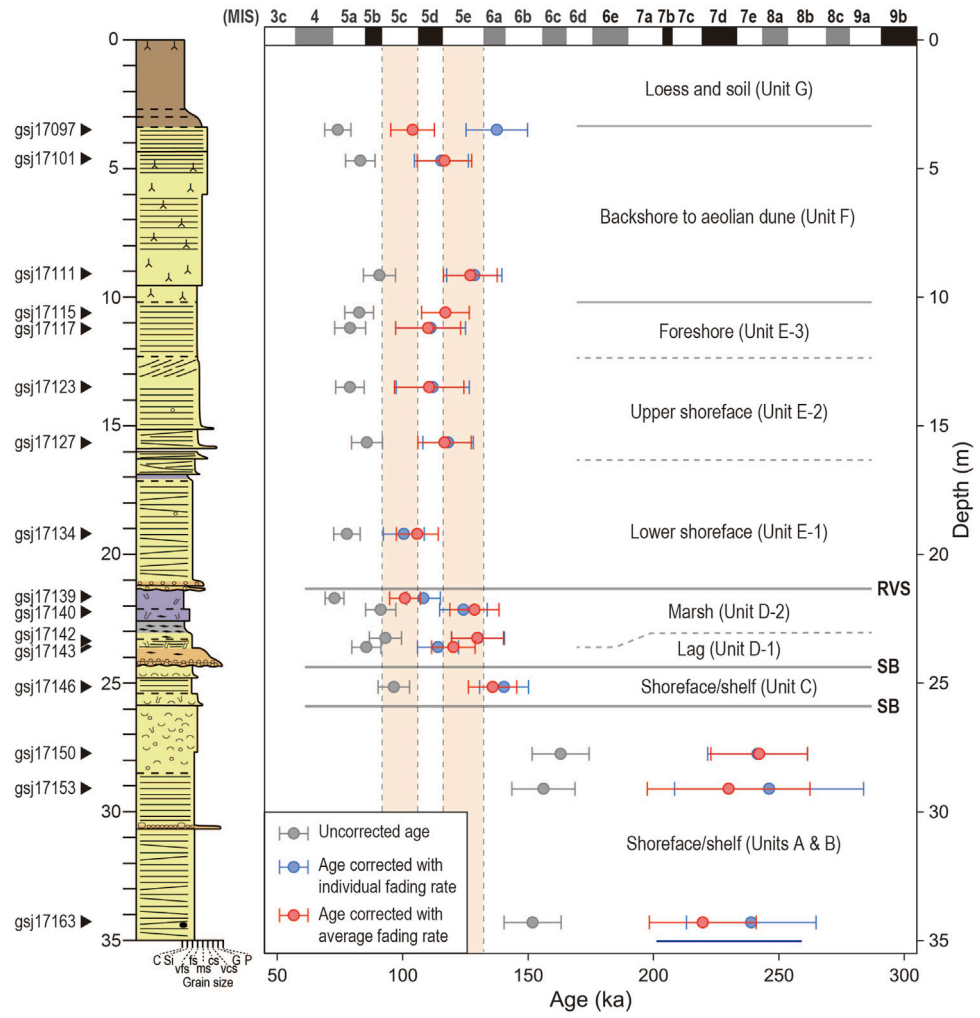

FIGURE 7
Plots of uncorrected and corrected pIRIR$_{225}$ ages of 16 samples in core GS-HKT-1 against core depth. The invervals of MIS 5c and 5e are shaded. The color legend of the core is shown in Figure 2.

lowstand and rise from MIS 5d to 5c resulted in unit D and the overlying ravinement surface. This constrains unit E, with MIS 5e to 5c pIRIR$_{225}$ ages, to represent coastal progradation during the MIS 5c sea-level highstand, followed by aeolian sedimentation of unit F. The marine terrace in the Kashima upland (Figure 1C) is thus correlated with MIS 5c similarly to Ooi et al. (2013), who considered the presence of the MIS 5c marine terrace in the seaward part of the Kashima upland according to tephras.

A diagram is presented in Figure 8 for plotting the corrected and residual-subtracted pIRIR$_{225}$ ages of individual samples against the sample elevation. As most samples were collected from deposits of underwater environments, the overestimation of pIRIR$_{225}$ ages owing to the residual dose is expected. Here, for all samples, the residual dose is assumed as the average determined for pIRIR$_{225}$ signal from the modern samples in the Kujukuri coast (8.83 ± 3.06 Gy; Table 2). The residual dose is divided by an average dose rate of 16 samples in core GS-HKT-1 (2.11 ± 0.17 Gy/ka; Table 1) to obtain possible age overestimation, 4,200 ± 150 years. The possible overestimation is then subtracted from the corrected pIRIR$_{225}$ ages. Even with the residual dose considered, individual ages appear slightly older than MIS that they are correlated with. Potential factors to cause such inaccuracy may include higher residual doses than assumed here and/or uncertainties in the dose rate, especially owing to temporal fluctuations of water content. These factors are not predictable, limiting further accuracy of the age estimate. Nevertheless, the application of pIRIR$_{225}$ dating to core GS-HKT-1 exemplifies how the information of sedimentary facies is used as an additional constraint for providing an accurate

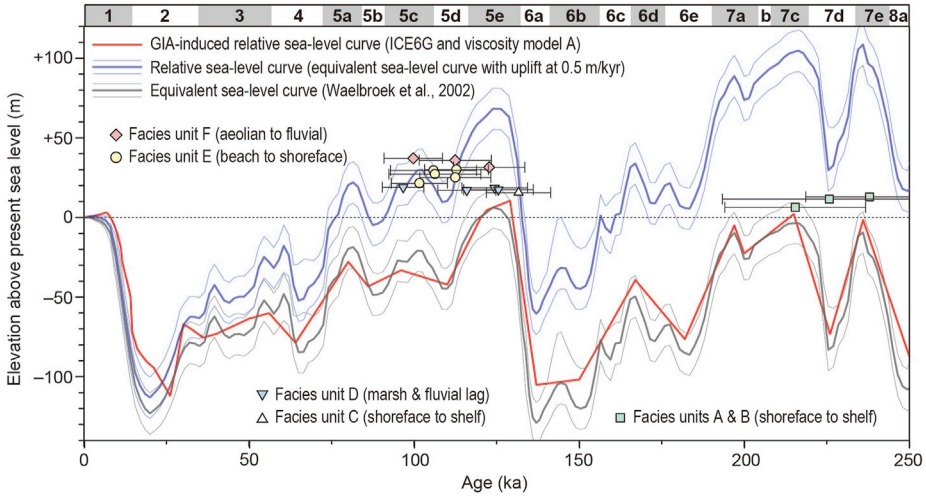

FIGURE 8
Sea-level curves compared with the plots of $pIRIR_{225}$ ages and elevations of samples in core GS-HKT-1. An expected age overestimate due to the residual dose, estimated as 4.2 ± 1.5 kyr, was subtracted from the $pIRIR_{225}$ ages (corrected with the average fading rate). The blue line represents a relative sea-level curve with an uplift rate of 0.5 m/kyr, which assumes the upper boundary of Unit E (or subunit E-3, foreshore facies) represents the sea-level highstand of the MIS 5c. GIA (Glacial Isostatic Adjustment)-induced relative sea-level curve was calculated based on the deglaciation model ICE6G_C (Argus et al., 2014). In order to have one cycle ice history only in ICE6G_C, the pre-history of equivalent sea-level changes before 122 ka was adopted from Waelbroeck et al., 2002. The viscosity model (model A) adopted here assumes that the elastic thickness is 50 km and the upper and lower mantle viscosities are 2×10^{20}, 2×10^{22} Pa s, respectively (Okuno et al., 2014).

chronology to identify high-frequency Pleistocene depositional sequences.

Tectonic uplift and relative sea-level changes

The revised chronology of the marine terrace in the eastern Kanto plain, as proposed in the Kashima upland here and the Iioka upland by Okazaki et al. (2022), refines the rate of the tectonic uplift. While units A, B, C, D-2, and E were deposited around or below the sea level, their age-elevation plots are far above the eustatic sea-level curve (Waelbroeck et al., 2002). This was resulted from the regional uplift owing both to the hydro-isostacy and tectonics. As the Kanto plain is in a far field, its GIA (Glacial Isostatic Adjustment)-induced relative sea level is not significantly offset from an eustatic sea level (Figure 8; Okuno et al., 2014). Thus, the regional uplift is dominated by the tectonic component. The elevation range of unit E-3, +28.4–30.5 m, is approximately indicative of the relative sea level during the MIS 5c highstand (Tamura, 2012), although the level of the corresponding shoreline angle may be somewhat higher. Assuming that the MIS 5c sea-level highstand occurred at 100 ka and was lower than that in MIS 5e (8 ± 5 m; Okuno et al., 2014) by 25 m (De Gelder et al., 2020), an uplift has occurred at the core site by 46.5 ± 5.1 m over the last 100 kyr, which gives the average uplift rate 0.46 ± 0.05 m/kyr, considerably higher than the rate inferred from the marine terrace correlation with MIS 5e, 0.17 ± 0.04 m/kyr, when an uplift is assumed to have occurred by 21.5 ± 5.1 m during 125 kyr. Similar refinement in the Iioka upland yields a rate of 0.70 ± 0.06 m/kyr (Okazaki et al., 2022), indicating spatial variations. Further refinement elsewhere in the Kanto plain should clarify the crustal displacement with higher accuracies and improve the understanding of the regional tectonics (Figure 1B; Kaizuka, 1987).

Extrapolation of the tectonic uplift rate, c. 0.5 m/kyr, to MIS 8a characterizes the relative sea-level curve and estimates the paleo-water depths of facies units (Figure 8). Age-elevation plots of units D and E occur around the contemporary relative sea level, consistent with their sedimentary environments. Unit C is considered to have been deposited at water depths of a few meters to 50 m. The paleo-water depths of units A and B are estimated to be up to 100 m. In the modern shelf off the Kujukuri coast, very fine to fine sand > 1 m thick was deposited after the mid Holocene at water depths up to 124 m (Nishida et al., 2020), much below the storm–wave base (c. 50–60 m; Tamura et al., 2008b). The sand deposition is interpreted to have been caused by the ocean current (Nishida et al., 2020). Units A and B in contrast show clear features of storm-wave deposition, such as hummocky and swaly cross stratifications, and thus were likely formed above the storm–wave base. The shallow-water deposition of units A and B could have been enabled by the significant sea-level fall around MIS 7d. The gravel layer that

separates units A-1 and A-2 possibly records an erosional episode enhanced by the sea-level fall. Otherwise, the relative sea-level curve constructed with the extrapolation of the tectonic uplift may not be valid. The extrapolation requires a temporally consistent tectonic displacement after MIS 7, which is not evident given the unique setting of the Kanto plain with the history of the long-term subsidence in contrast to the ongoing uplift.

Conclusions

We examine the effectiveness of feldspar $pIRIR_{225}$ dating for identifying terrigenous, coastal, and shallow-marine depositional sequences since the Middle Pleistocene, observed in a 35-m-long sediment core from the Last Interglacial-raised marine terrace in the northeastern Kanto plain, a unique Quaternary forearc basin near the triple junction of the plate boundaries. Sixteen fading-corrected $pIRIR_{225}$ ages define a large hiatus spanning MIS 6 and are useful for separating the intervals of MIS 5 and MIS 7. Their uncertainties, however, do not allow further detailed correlation. The sediment facies succession in the core shows some key features representing shifts from shallow-marine to fluvial environments and from fluvial to brackish salt marsh and coastal progradation. Sea-level oscillations inferred from these features can be used for constraining the chronology of the higher-frequency sequences in the MIS 5 interval. Our results exemplify an effective combination of luminescence dating with stratigraphic information for detailed chronological interpretation. The luminescence chronology of the sediment core also refines the date of the marine terrace and revises up the rate of local tectonic uplift. Further application of feldspar pIRIR dating to the Kanto plain likely improves our understanding of the unique tectonic history.

Data availability statement

The original contributions presented in the study are included in the article/Supplementary Material; further inquiries can be directed to the corresponding author.

Author contributions

TT designed the study. TT, HO, HN, and KS analyzed the sediment cores. RN identified species of mollusk shells. TN identified species of diatoms. KS identified trace fossils. TT carried out the luminescence dating and wrote the manuscript. HO, TN, RN, HN, KS, and JO contributed to the discussion and commented on the manuscript. All authors reviewed and approved the final version of the manuscript.

Funding

This study was funded by Grant-in-Aid for Scientific Research (B) (No. 18H01294) from the Japan Society for the Promotion of Science to Toru Tamura and an internal grant from the Geological Survey of Japan, AIST.

Acknowledgments

We express our gratitude to Kana Takamori for her fundamental laboratory assistance. Kumi Yokoi is also thanked for obtaining radiographs. The manuscript was significantly improved by reviewers Xiaomei Nian and Xianjiao Ou, and journal editor Hao Long.

Conflict of interest

The authors declare that the research was conducted in the absence of any commercial or financial relationships that could be construed as a potential conflict of interest.

Publisher's note

Supplementary material

The Supplementary Material for this article can be found online at: https://www.frontiersin.org/articles/10.3389/feart.2022.967572/full#supplementary-material

References

Adamiec, G., and Aitken, M. (1998). Dose-rate conversion factors: Update. *Anc. TL* 16, 37–50.

Argus, D. F., Peltier, W. R., Drummond, R., and Moore, A. W. (2014). The Antarctica component of postglacial rebound model ICE-6G_C (VM5a) based on GPS positioning, exposure age dating of ice thicknesses, and relative sea level histories. *Geophys. J. Int.* 198, 537–563. doi:10.1093/gji/ggu140

Arnold, L. J., Demuro, M., Pares, J. M., Arsuaga, J. L., Aranburu, A., de Castro, J. M. B., et al. (2014). Luminescence dating and palaeomagnetic age constraint on

hominins from Sima de los Huesos, Atapuerca, Spain. *J. Hum. Evol.* 67, 85–107. doi:10.1016/j.jhevol.2013.12.001

Auclair, M., Lamothe, M., and Huot, S. (2003)). Measurement of anomalous fading for feldspar IRSL using SAR. *Radiat. Meas.* 37, 487–492. doi:10.1016/S1350-4487(03)00018-0

Balescu, S., and Lamothe, M. (1994). Comparison of TL and IRSL age estimates of feldspar coarse grains from waterlain sediments. *Quat. Sci. Rev.* 13, 437–444. doi:10.1016/0277-3791(94)90056-6

Bell, W. T. (1980). Alpha dse attenuation in quartz grains for thermoluminescence dating. *Anc. TL* 12, 4–8.

Buylaert, J. P., Murray, A. S., Thomsen, K. J., and Jain, M. (2009). Testing the potential of an elevated temperature IRSL signal from K-feldspar. *Radiat. Meas.* 44, 560–565. doi:10.1016/j.radmeas.2009.02.00710.1016/j.radmeas.2009.02.007

Buylaert, J. P., Murray, A. S., Gebhardt, A. C., Sohbati, R., Ohlendorf, C., Thiel, C., et al.The PASADO Science Team (2013). Luminescence dating of the PASADO core 5022-1D from Laguna Potrok Aike (Argentina) using IRSL signals from feldspar. *Quat. Sci. Rev.* 71, 70–80. doi:10.1016/j.quascirev.2013.03.018

Christ, A. J., Bierman, P. R., Schaefer, J. M., Dahl-Jensen, D., Steffensen, J. P., Corbett, L. B., et al. (2021). A multimillion-year-old record of Greenland vegetation and glacial history preserved in sediment beneath 1.4 km of ice at Camp Century. *Proc. Natl. Acad. Sci. U. S. A.* 118, e2021442118. doi:10.1073/pnas.2021442118

Clifton, H. E. (2006). "A reexamination of facies models for clastic shorelines," in *Facies models revisited*. Editors H. W. Posamentier and R. G. Walker (Oklahoma, United States: SEPM Spec. Publ.), 84, 293–337.

De Gelder, G., Jara-Mu~noz, J., Melnick, D., Fern andez-Blanco, D., Rouby, H., Pedoja, K., et al. (2020). How do sea-level curves influence modeled marine terrace sequences? *Quat. Sci. Rev.* 229, 106132. doi:10.1016/j.quascirev.2019.106132

Durcan, J. A., King, G. E., and Duller, G. A. T. (2015). Drac: Dose rate and age calculator for trapped charge dating. *Quat. Geochronol.* 28, 54–61. doi:10.1016/j.quageo.2015.03.012

Fuchs, M. C., Kreutzer, S., Burow, C., Dietze, M., Fischer, M., Schmidt, C., et al. (2015). Data processing in luminescence dating analysis: An exemplary workflow using the R package 'luminescence. *Quat. Int.* 362, 8–13. doi:10.1016/j.quaint.2014.06.034

Harms, J. C., Southard, J. B., Spearing, D. R., and Walker, R. G. (1975). Depositional environments as interpreted from primary sedimentary structures and stratification sequences. *SEPM Short. Course* 2, 161.

Huntley, D. J., and Lian, O. B. (2006). Some observations on tunnelling of trapped electrons in feldspars and their implications for optical dating. *Quat. Sci. Rev.* 25, 2503–2512. doi:10.1016/j.quascirev.2005.05.011

Isla, M. F., Schwarz, E., and Veiga, G. D. (2020). Record of a nonbarred clastic shoreline. *Geology* 48, 338–342. doi:10.1130/g46800.1

Ito, M., and O'hara, S. (1994). Diachronous evolution of systems tracts in a depositional sequence from the middle Pleistocene palaeo-Tokyo Bay, Japan. *Sedimentology* 41, 677–697. doi:10.1111/j.1365-3091.1994.tb01417.x

Kaizuka, S. (1987). Quaternary crustal movements in Kanto, Japan. *J. Geogr.* 96, 223–240. doi:10.5026/jgeography.96.4_223

Kars, R. H., Wallinga, J., and Cohen, K. M. (2008). A new approach towards anomalous fading correction for feldspar IRSL dating—Tests on samples in field saturation. *Radiat. Meas.* 43, 786–790. doi:10.1016/j.radmeas.2008.01.021

Kreutzer, S., Schmidt, C., DeWitt, R., and Fuchs, M. (2014). The a-value of polymineral fine grain samples measured with the post-IR IRSL protocol. *Radiat. Meas.* 69, 18–29. doi:10.1016/j.radmeas.2014.04.027

Kreutzer, S., Schmidt, C., Fuchs, M. C., Dietze, M., Fischer, M., and Fuchs, M. (2012). Introducing an R package for luminescence dating analysis. *Anc. TL* 30, 1–8.

Leckie, D. A., and Walker, R. G. (1982). Storm-and tide-dominated shorelines in cretaceous moosebar-lower gates interval—Outcrop equivalents of deep basin gas trap in Western Canada. *AAPG Bull.* 66, 138–157.

Li, B., Jacobs, Z., Roberts, R. G., and Li, S. H. (2014). Review and assessment of the potential of post-IR IRSL dating methods to circumvent the problem of anomalous fading in feldspar luminescence. *Geochronometria* 41, 178–201. doi:10.2478/s13386-013-0160-3

Li, B., and Li, S. H. (2012). Luminescence dating of Chinese loess beyond 130 ka using the non-fading signal from K-feldspar. *Quat. Geochronol.* 10, 24–31. doi:10.1016/j.quageo.2011.12.005

Li, Z. Y., Wu, X. J., Zhou, L. P., Liu, W., Gao, X., Nian, X. M., et al. (2017). Late Pleistocene archaic human crania from Xuchang, China. *Science* 355, 969–972. doi:10.1126/science.aal2482

Lisiecki, L. E., and Raymo, M. E. (2005). A Pliocene-Pleistocene stack of 57 globally distributed benthic $\delta^{18}O$ records. *Paleoceanography* 20, PA1003. doi:10.1029/2004PA001071

Machida, H., and Arai, F. (2003). *Atlas of tephra in and around Japan*. Tokyo: University of Tokyo Press, 336.

Mejdahl, V. (1979). Thermoluminescence dating: Beta-dose attenuation in quartz grains. *Archaeometry* 21, 61–72. doi:10.1111/j.1475-4754.1979.tb00241.x

Murakoshi, N., and Masuda, F. (1992). Estuarine, barrier-island to strand-plain sequence and related ravinement surface developed during the last interglacial in the Paleo-Tokyo Bay, Japan. *Sediment. Geol.* 80, 167–184. doi:10.1016/0037-0738(92)90039-t

Murray, A. S., Schmidt, E. D., Stevens, T., Buylaert, J. P., Marković, S. B., Tsukamoto, S., et al. (2014). Dating middle pleistocene loess from stari slankamen (vojvodina, Serbia)—Limitations imposed by the saturation behaviour of an elevated temperature IRSL signal. *Catena* 117, 34–42. doi:10.1016/j.catena.2013.06.029

Murray-Wallace, C. V., and Woodroffe, C. D. (2014). *Quaternary sea level changes: A global perspective*. Cambridge: Cambridge University Press, 484.

Nakazawa, T., Sakata, K., Hongo, M., and Nakazato, H. (2017). Transition from incised valley to barrier island systems during MIS 5e in the northern Chiba area, Kanto Plain, central Japan. *Quat. Int.* 456, 85–101. doi:10.1016/j.quaint.2017.06.031

Nakazato, H., and Sato, H. (2001). sea level changes and tectonics inferred from the quaternary deposits and landforms of Boso Peninsula, central Japan. Chronology of the Shimosa Group and movement of the Kashima uplift zone, central Japan. *Daiyonki-kenkyu.* 40, 251–257. doi:10.4116/jaqua.40.251

Naya, T. (2019). Stratigraphic distribution and biostratigraphic utility of the fossil diatom *Lancineis rectilatus* in the central Kanto Plain, central Japan. *Quat. Int.* 519, 131–143. doi:10.1016/j.quaint.2018.11.002

Nian, X., Li, F., Chen, F., Zhang, W., Zhao, Y., Zhou, J., et al. (2016). Optically stimulated luminescence ages for human occupation during the penultimate glaciation in the Western Loess Plateau of China. *J. Quat. Sci.* 31, e2917. doi:10.1002/jqs.2917

Nishida, N., Ajioka, T., Ikehara, K., Nakashima, R., Katayama, H., Sato, T., et al. (2020). Postglacial stratigraphic evolution of a current-influenced sandy shelf: Offshore Kujukuri strandplain, central Japan. *Sedimentology* 67, 559–575. doi:10.1111/sed.12654

Nishida, N., and Ito, M. (2009). Fluid mud: Distinctive features and implications for genetic stratigraphy. *Jour. Geol. Soc. Jpn.* 115, 149–167. doi:10.5575/geosoc.115.149

Nummedal, D., and Swift, D. J. P. (1987). "Transgressive stratigraphy at sequence-bounding unconformities: Some principles derived from Holocene and cretaceous examples,". Editors D. Nummedal, O. H. Pilkey, and J. D. Howard (Oklahoma, United States: SEPM Spec. Publ.), 41, 241–260.*Sea-level Fluctuation Coast. Evol.*

Okazaki, H., and Masuda, F. (1992). Depositional systems of the late pleistocene sediments in paleo-Tokyo bay area. Ko tokyowan chiiki no taiseki system. *J. Geol. Soc. Jpn.* 98, 235–258.

Okazaki, H., Nara, M., Nakazato, H., Furusawa, A., Ito, K., Tamura, T., et al. (2022). Coastal progradation associated with sea-level oscillations in the later phase of the Last Interglacial period, central Japan. *Quat. Sci. Rev.* 285, 107507. doi:10.1016/j.quascirev.2022.107507

Okazaki, H., Sato, H., and Nakazato, H. (1997). Two types of depositional sequences developed in paleo-tokyo bay, exampled from the Kamiizumi, Kiyokawa and Yokota formations, pleistocene Shimosa Group, Japan. *Jour. Geol. Soc. Jpn.* 103, 1125–1143. doi:10.5575/geosoc.103.1125

Okuno, J., Nakada, M., Ishii, M., and Miura, H. (2014). Vertical tectonic crustal movements along the Japanese coastlines inferred from late Quaternary and recent relative sea-level changes. *Quat. Sci. Rev.* 91, 42–61. doi:10.1016/j.quascirev.2014.03.010

Okutani, T. (2000). *Marine mollusks in Japan*. Tokyo: Tokai University Press, 1173.

Ooi, S., Sairenji, N., Yokoyama, Y., and Ando, H. (2013). Re-examination of terrace surface division of the Hitachi terraces, Ibaraki Prefecture. *Bull. Ibaraki Nat. Mus.* 16, 51–56.

Prescott, J. R., and Hutton, J. T. (1994). Cosmic ray contributions to dose rates for luminescence and ESR dating: Large depths and long-term time variations. *Radiat. Meas.* 23, 497–500. doi:10.1016/1350-4487(94)90086-8

Railsback, L. B., Gibbard, P. L., Head, M. J., Voarintsoa, N. R. G., and Toucanne, S. (2015). An optimized scheme of lettered marine isotope substages for the last 1.0 million years, and the climatostratigraphic nature of isotope stages and substages. *Quat. Sci. Rev.* 111, 94–106. doi:10.1016/j.quascirev.2015.01.012

Reimann, T., and Tsukamoto, S. (2012). Dating the recent past (< 500 years) by post-IR IRSL feldspar–examples from the north sea and baltic sea coast. *Quat. Geochronol.* 10, 180–187. doi:10.1016/j.quageo.2012.04.011

Rizal, Y., Westaway, K. E., Zaim, Y., van den Bergh, G. D., Bettis, E. A., Morwood, M. J., et al. (2020). Last appearance of Homo erectus at Ngandong, Java, 117, 000–108, 000 years ago. *Nature* 577, 381–385. doi:10.1038/s41586-019-1863-2

Sohbati, R., Murray, A. S., Buylaert, J. P., Ortuño, M., Cunha, P. P., Masana, E., et al. (2012). Luminescence dating of P leistocene alluvial sediments affected by the A lhama de M urcia fault (eastern B etics, S pain)–a comparison between OSL, IRSL and post-IR IRSL ages. *Boreas* 41, 250–262. doi:10.1111/j.1502-3885.2011.00230.x

Stevens, T., Buylaert, J. P., Thiel, C., Újvári, G., Yi, S., Murray, A. S., et al. (2018). Ice-volume-forced erosion of the Chinese Loess Plateau global Quaternary stratotype site. *Nat. Commun.* 9, 983. doi:10.1038/s41467-018-03329-2

Stevens, T., Marković, S. B., Zech, M., Hambach, U., and Sümegi, P. (2011). Dust deposition and climate in the Carpathian Basin over an independently dated last glacial–interglacial cycle. *Quat. Sci. Rev.* 30, 662–681. doi:10.1016/j.quascirev.2010.12.011

Sugai, T., Matsushima, H., and Mizuno, K. (2013). Last 400 ka landform evolution of the Kanto Plain: Under the influence of concurrent glacio-eustatic sea level changes and tectonic activity. *J. Geogr.* 122, 921–948. doi:10.5026/jgeography.122.921

Sugihara, S. (1970). Geomorphological developments gp the western shimôsa upland in chiba prefecture, Japan. *Geogr. Rev. Jpn.* 43, 703–718. doi:10.4157/grj.43.703

Suzuki, H., and Tango, T. (2002). A multicenter, randomized, controlled clinical trial of interferon alfacon-1 in comparison with lymphoblastoid interferon-alpha in patients with high-titer chronic hepatitis C virus infection. *Hepatol. Res.* 63, 1–12. doi:10.1016/s1386-6346(01)00139-5

Suzuki, T., Obara, M., Aoki, T., Murata, M., Kawashima, S., Kawai, M., et al. (2011). Identification of lower pleistocene tephras under Tokyo and reconstruction of quaternary crustal movements, Kanto tectonic basin, central Japan. *Quat. Int.* 246, 247–259. doi:10.1016/j.quaint.2011.06.043

Takahashi, M., Hayashi, H., Kasahara, K., Ikawa, T., Kawanaka, T., and Suda, S. (2005). Miocene subsurface half-grabens in the Kanto plain, central Japan. *Rep. Nat. Res. Inst. Ear. Sci. Disast. Prev.* 67, 65–74.

Tamura, T. (2012). Beach ridges and prograded beach deposits as palaeoenvironment records. *Earth. Sci. Rev.* 114, 279–297. doi:10.1016/j.earscirev.2012.06.004

Tamura, T., Komatsubara, J., Sugisaki, S., and Nishida, N. (2021). Residual dose of K-feldspar post-IR IRSL of beach-shoreface sands at Kujukuri, eastern Japan. *Geochronometria* 48, 364–378. doi:10.2478/geochr-2020-0036

Tamura, T., and Masuda, F. (2005). Bed thickness characteristics of inner-shelf storm deposits associated with a transgressive to regressive Holocene wave-dominated shelf, Sendai coastal plain, Japan. *Sedimentology* 52, 1375–1395. doi:10.1111/j.1365-3091.2005.00745.x

Tamura, T., Masuda, F., Sakai, T., and Fujiwara, O. (2003). Temporal development of prograding beach–shoreface deposits: The Holocene of Kujukuri coastal plain, eastern Japan. *Mar. Geol.* 198, 191–207. doi:10.1016/s0025-3227(03)00123-3

Tamura, T., Murakami, F., Nanayama, F., Watanabe, K., and Saito, Y. (2008a). Groundpenetrating radar profiles of Holocene raised-beach deposits in the Kujukuri strand plain, Pacific coast of eastern Japan. *Mar. Geol.* 248, 11–27. doi:10.1016/j.margeo.2007.10.002

Tamura, T., Nanayama, F., Saito, Y., Murakami, F., Nakashima, R., Watanabe, K., et al. (2007). Intra-shoreface erosion in response to rapid Sea-level fall: Depositional record of a tectonically uplifted strand plain, pacific coast of Japan. *Sedimentology* 54, 1149–1162. doi:10.1111/j.1365-3091.2007.00876.x

Tamura, T., Saito, Y., and Masuda, F. (2008b). "Variations in depositional architecture of Holocene to modern prograding shorefaces along the Pacific coast of eastern Japan," in *Recent advances in models of siliciclastic shallow-marine stratigraphy*. Editors G. J. Hampson, R. J. Steel, P. Burgess, and R. W. Dalrymple (Oklahoma, United States: SEPM Spec. Publ), 90, 189–203.

Thiel, C., Buylaert, J. P., Murray, A., Terhorst, B., Hofer, I., Tsukamoto, S., et al. (2011). Luminescence dating of the Stratzing loess profile (Austria)–Testing the potential of an elevated temperature post-IR IRSL protocol. *Quat. Int.* 234, 23–31. doi:10.1016/j.quaint.2010.05.018

Thomsen, K. J., Murray, A. S., Jain, M., and Bøtter-Jensen, L. (2008). Laborato-ry fading rates of various luminescence signals from feldspar-rich sediment extracts. *Radiat. Meas.* 43, 1474–1486. doi:10.1016/j.radmeas.2008.06.002

Tokuhashi, S., and Kondo, Y. (1989). Sedimentary cycles and environments in the middle-late pleistocene Shimosa Group, Boso Peninsula, central Japan. *Jour. Geol. Soc. Jpn.* 95, 933–951. doi:10.5575/geosoc.95.933

Waelbroeck, C., Labeyrie, L., Michel, E., Duplessy, J. C., Mcmanus, J. F., Lambeck, K., et al. (2002). Sea-level and deep water temperature changes derived from benthic foraminifera isotopic records. *Quat. Sci. Rev.* 21, 295–305. doi:10.1016/s0277-3791(01)00101-9

Westaway, K. E., Louys, J., Awe, R., Morwood, M. J., Price, G. J., Zhao, J. X., et al. (2017). An early modern human presence in Sumatra 73, 000–63, 000 years ago. *Nature* 548, 322–325. doi:10.1038/nature23452